OPEN ACCESS

ACTA METALLURGICA SLOVACA

2026, VOL. 32, NO. 2, 155-162

SCICELL

RESEARCH PAPER

Microstructural and phase evolution of Ti-6Al-4V alloy produced by laser powder bed fusion (LPBF) under electron irradiation

Yerik Merkibayev[1], Tatyana Chepushtanova[1], Bauyrzhan Bazarbay[1], Arailym Berlibek[1], Kulzira Mamyrbaeva[1], Pavel Sherstnev[2], Christof Sommitsch[3]*

[1]Department of Mechanical Engineering, Metallurgy and Mineral Processing, Satbayev University, Almaty, Kazakhstan.
[2]Sherstnev group LLC, Almaty, Kazakhstan.
[3]Institute of Materials Science, Joining and Forming, Graz University of Technology, Austria.

*Corresponding author: b.bazarbay@satbayev.university, tel.: +7 747 708 7652, Department of Mechanical Engineering, Satbayev University, 050010, Almaty, Kazakhstan.

Received: 18.05.2026
Accepted: 09.06.2026

ABSTRACT

In this paper, the microstructural, chemical, and phase evolution of a Ti-6Al-4V alloy fabricated by Laser Powder Bed Fusion (LPBF) and subsequently subjected to electron irradiation was investigated. The LPBF process results in the formation of a nonequilibrium microstructure under rapid solidification conditions (≈10^5–10^6 K/s), including acicular α′-martensite, oriented prior β grains, and microporosity (≈0.2–1.0 μm). Scanning electron microscopy (SEM), energy-dispersive spectroscopy (EDS), and X-ray diffraction (XRD) were employed to characterize the material before and after irradiation. SEM observations revealed that electron irradiation increased the agglomerate size from approximately 50–100 μm to 70–150 μm, while reducing pore size from 0.2–1.0 μm to 0.05–0.6 μm. EDS analysis indicated a decrease in Ti content accompanied by an increase in oxygen and carbon concentrations, suggesting surface oxidation and chemical modification. XRD analysis confirmed the transformation of the initial Al–Ti intermetallic phases and the predominance of the hexagonal Ti phase after irradiation. Changes in lattice parameters (a: 2.927→2.936 Å; c: 4.663→4.676 Å) indicate lattice expansion and redistribution of internal stresses. The obtained results demonstrate that electron irradiation significantly affects the structural state of LPBF-fabricated Ti-6Al-4V alloy and can be considered an effective approach for tailoring the process–structure–property relationship in additively manufactured titanium alloys.

Keywords: Laser Powder Bed Fusion (LPBF); additive manufacturing; microstructure; phase transformation; X-ray diffraction; titanium alloy.

INTRODUCTION

The Ti-6Al-4V alloy is one of the most widely used structural materials among the α+β-type titanium alloys, characterized by high specific strength (≈900–1100 MPa), relatively low density (≈4.43 g/cm³), corrosion resistance, and biocompatibility [1–4]. Aluminum (≈6 wt.%) stabilizes the α-phase, while vanadium (≈4 wt.%) stabilizes the β-phase, providing an optimal balance between the strength and plasticity of the material [5–7]. This combination of properties allows this alloy to be widely used in aviation, medicine, and highly loaded structures.

According to ASTM F3187 terminology, the manufacturing process used in this study is classified as Laser Powder Bed Fusion (LPBF), which belongs to the broader category of Additive Manufacturing (AM). LPBF is currently one of the most widely used additive manufacturing technologies for producing metallic components with complex geometries, high dimensional accuracy, and reduced material waste [8–11].This method is based on the formation of a layer-by-layer structure by melting thin layers (≈20–50 μm) of metal powders under the influence of high-energy laser radiation. The LPBF process involves very high temperature gradients (≈10^5–10^6 K/s) and high cooling rates, which lead to the formation of a no equilibrium and metastable microstructure. [12–15].

According to the literature, LPBF-fabricated Ti-6Al-4V alloy exhibits an acicular α′-martensitic structure, oriented prior β grains, and residual porosity [16–19]. Although such a structure contributes to high strength, it can reduce its ductility and fatigue strength by ≈15–30% [20–22]. In addition, residual thermal stresses and process defects (e.g., lack of fusion and gas pores) formed during production disrupt the material's structural homogeneity and adversely affect its performance properties [23,24]. Post-processing methods are widely used to mitigate these problems. In particular, heat treatment ensures the decomposition of α′-martensite into a stable α+β phase structure, reduces residual stresses by ≈40–60%, and improves the plastic properties of the material [25–28]. However, in recent years, research has been intensively developing in the direction of using radiation effects along with traditional methods for targeted control of the structure.

One such promising method is electron irradiation. This method accelerates high-energy electrons in a vacuum environment and interacts with the surface layer of the material. This activates atomic diffusion processes, reorganizes the dislocation structure, and causes resintering due to local thermal effects [29–31]. Furthermore, the accumulation of energy in the surface layer during irradiation leads to pore closure, structural compaction, and morphological smoothing [32–34].

In this study, electron irradiation was performed in a dedicated vacuum setup, where the operating pressure was maintained at ≈1.3×10^{-2} Pa. The electron beam was generated at an accelerating voltage of 10 kV, and the power supply was supplied with a voltage of ≈127 V. These parameters ensure free electron movement and allow for the efficient concentration of energy on the material's surface, thereby enhancing microstructural reorganization processes.

Studies have shown that electron irradiation increases the size of agglomerates from 50–100 μm to 70–150 μm (≈20–40%), while porosity decreases from 0.2–1.0 μm to 0.05–0.6 μm (≈40–60%). At the same time, the size of nanostructured elements changes from 50–200 nm to 30–120 nm, and the degree of their integration increases, which is explained by a decrease in atomic diffusion and surface energy [35]. The combination of additive manufacturing and radiation processing opens up new possibilities for controlling the process–structure–property relationship of a material. However, the patterns of structural and phase changes in the Ti-6Al-4V alloy obtained by LPBF under electron irradiation have not yet been fully studied.

The aim of this work is to comprehensively study the structural and phase evolution of the Ti-6Al-4V alloy fabricated by LPBF technology, as well as to quantitatively and qualitatively determine the effect of electron irradiation and heat treatment on the microstructure, phase composition and functional properties of the material. The scientific novelty of this work lies in the comprehensive investigation of the combined effect of electron irradiation and heat treatment on the structural and phase evolution of LPBF-fabricated Ti-6Al-4V alloy. Unlike previous studies, where thermal treatment and irradiation effects were mainly considered separately, this study evaluates their combined influence on α′-martensite transformation, pore evolution, microstructural densification, and morphological modification. The obtained results provide new insights into the relationship between irradiation-induced structural changes and the phase state of additively manufactured Ti-6Al-4V alloy.

MATERIAL AND METHODS

Ti-6Al-4V (α+β type) fabricated by LPBF)

The specimens used in this study were prepared from Ti-6Al-4V titanium alloy (α+β type) using Laser Powder Bed Fusion (LPBF).A total of five specimens were fabricated and investigated in this study. One specimen was characterized in the as-fabricated condition, while four specimens were subjected to electron irradiation under identical processing conditions. The investigated samples were produced from the same batch of Ti-6Al-4V powder and manufactured using identical LPBF parameters to ensure the reproducibility and reliability of the experimental results. To ensure reproducibility, the electron irradiation experiments were repeated on multiple specimens under identical processing conditions, including accelerating voltage, irradiation time, and vacuum level. SEM, EDS, and XRD analyses demonstrated consistent trends in microstructural evolution, porosity reduction, and phase transformation among the investigated samples, confirming the reproducibility of the obtained results. The starting material was gas-atomized Ti-6Al-4V powder with a spherical morphology and high flowability, with a particle size in the range of approximately 15–45 μm. The powder chemical composition was maintained within a standard range (≈6 wt% Al and ≈4 wt% V), which ensures stabilization of the α- and β-phases.

The selection of the LPBF processing parameters was based on the requirement. The powder fraction of 15–45 μm was selected due to its high flowability and ability to form uniform powder layers during recoating. A layer thickness of 30–40 μm was chosen to ensure complete melting of powder particles and to reduce the probability of lack-of-fusion defects. The manufacturing process was carried out in an argon atmosphere with an oxygen content below 0.1% to minimize oxidation of titanium during laser processing. The laser power was maintained at approximately 200 W, the scanning speed at 1200 mm/s, and the hatch spacing at 100 μm. These parameters provided sufficient volumetric energy density for complete melting of the powder while preventing overheating, excessive evaporation of alloying elements, and keyhole formation. All samples were fabricated using identical processing conditions to ensure the reproducibility of the experimental results.

During LPBF processing, the layer thickness was selected at ≈30–40 μm, and the powder layers were melted layer by layer under laser irradiation, forming a structure under high-speed crystallization conditions. The LPBF process can cause the accumulation of residual thermal stresses and the formation of process defects (gas pores, lack of fusion). The resulting samples were subsequently processed by electron irradiation using a high-energy electron beam. Electron irradiation was performed in a vacuum system at the laboratories of Satbayev University (Almaty, Kazakhstan), where the operating pressure was maintained at ≈1.3×10^{-2} Pa.

Fig. 1 Electron irradiation period

During irradiation, the accelerating voltage was set at 10 kV, and a voltage of approximately 127 V was supplied to the power system via a LATR. The irradiation time was set at 20–30 minutes, ensuring sufficient energy accumulation on the surface layer of the material.

The electron irradiation process was carried out under conditions providing stable beam propagation in a vacuum environment. The irradiation was performed in a continuous mode without pulse modulation of the electron beam. The accelerating voltage was maintained at 10 kV throughout the experiment, while the estimated beam current was in the range of 5–10 mA. The effective beam spot diameter on the sample surface was approximately 5–10 mm, corresponding to an estimated current density of 6–50 mA·cm^{-2} depending on the irradiated area. The exposure time varied from 20 to 30 min, resulting in a total energy input sufficient to induce structural modifications within the near-surface layer of the material. The absorbed dose was estimated to be on the order of 10^2–10^3 kGy, which is consistent with values typically used for electron-beam surface modification of metallic materials. Under these conditions, the irradiation treatment ensured localized energy deposition, activation of diffusion processes, redistribution of crystal defects, and structural relaxation phenomena.

In these conditions, electrons are freely accelerated in a vacuum environment and intensively interact with the surface layer of the sample. This results in a localized thermal effect and a significant increase in temperature, which was experimentally recorded as a glow (intense glow) in the irradiated zone of the sample. These conditions accelerate atomic diffusion, structural relaxation, and resintering processes. Furthermore, the interaction of electrons with the crystal lattice ensures the redistribution of defects such as vacancies, interstitial atoms, and dislocations, which facilitates microstructural reorganization and material densification. As a result, porosity decreases, the degree of coalescence of agglomerates increases, and the surface morphology is smoothed.

Scanning electron microscopy (SEM) was used to study the morphological characteristics of the samples. The studies were carried out using a TESCAN VEGA 3 LMU scanning electron microscope at the Center of Engineering Competence of Satbayev University (Almaty, Kazakhstan) at an accelerating voltage of 10 kV and an electron beam current of 0.37 nA. The working distance was maintained in the range of 7–10 mm. To fully evaluate the surface structure of the sample, a magnification range of 100× to 10,000× was used. The morphology of the agglomerates, particle sizes, porosity structure, and the distribution of nanostructured elements were analyzed from SEM images. Energy-dispersive X-ray spectroscopy (EDS) was used to determine the elemental composition. The analysis was carried out using Oxford X-Max 20 Instruments EDS detector integrated into the SEM system. The measurements were performed at a voltage of 10 kV and a data collection time of ≈50–60 s. The atomic and mass fractions of Ti, Al, C, O, and trace elements were determined in accordance with the elemental composition. X-ray diffraction (XRD) was used to determine the phase composition. The measurements were carried out using Rigaku Ultima IV X-ray diffractometer at Satbayev University (Almaty, Kazakhstan) with Cu Kα radiation (λ = 1.5406 Å), at a voltage of 40 kV and a current of 15 mA. The diffraction spectrum was recorded in the range of 2θ = 3–90°, and the obtained results were used to identify the phases and calculate the lattice parameters. The XRD analysis was used primarily for phase identification and lattice parameter determination. Quantitative phase analysis using the Rietveld refinement method was not performed in the present study and will be considered in future investigations to obtain more detailed crystallographic information. Numerical processing of the experimental data allowed us to determine the structural parameters. According to scanning electron microscope (SEM) images, the agglomerate sizes were estimated to be in the range of ≈50–150 μm, particle sizes ≈1–20 μm, pore sizes ≈0.05–1.0 μm, and the sizes of nanostructured elements ≈30–200 nm. The pore size measurements were performed using digital image analysis of SEM micrographs. For each condition, at least 50 representative pores were measured from multiple SEM images acquired at different magnifications. The average pore size and pore size distribution were determined from the collected data. The reported porosity values correspond to the observed pore-size range within the analyzed surface regions. These parameters were compared before and after irradiation, and the patterns of structural evolution were determined. Thus, the complex of methods used (SEM, EDS, X-ray diffraction analysis) allows for a comprehensive characterization of the microstructure, elemental composition and phase state of the Ti-6Al-4V alloy obtained using LPBF technology, and the electron irradiation parameters allow for highly accurate tracking of morphological and structural changes in the material.

RESULTS AND DISCUSSION

Study Ti-6Al-4V using SEM, EDS, and X-ray diffraction

The structural and phase state of the Ti-6Al-4V alloy under study was comprehensively analyzed using SEM, EDS, and X-ray diffraction analysis in its initial state, after additive manufacturing, and after electron irradiation. Scanning electron microscopy results revealed clear differences between the structures before and after irradiation.

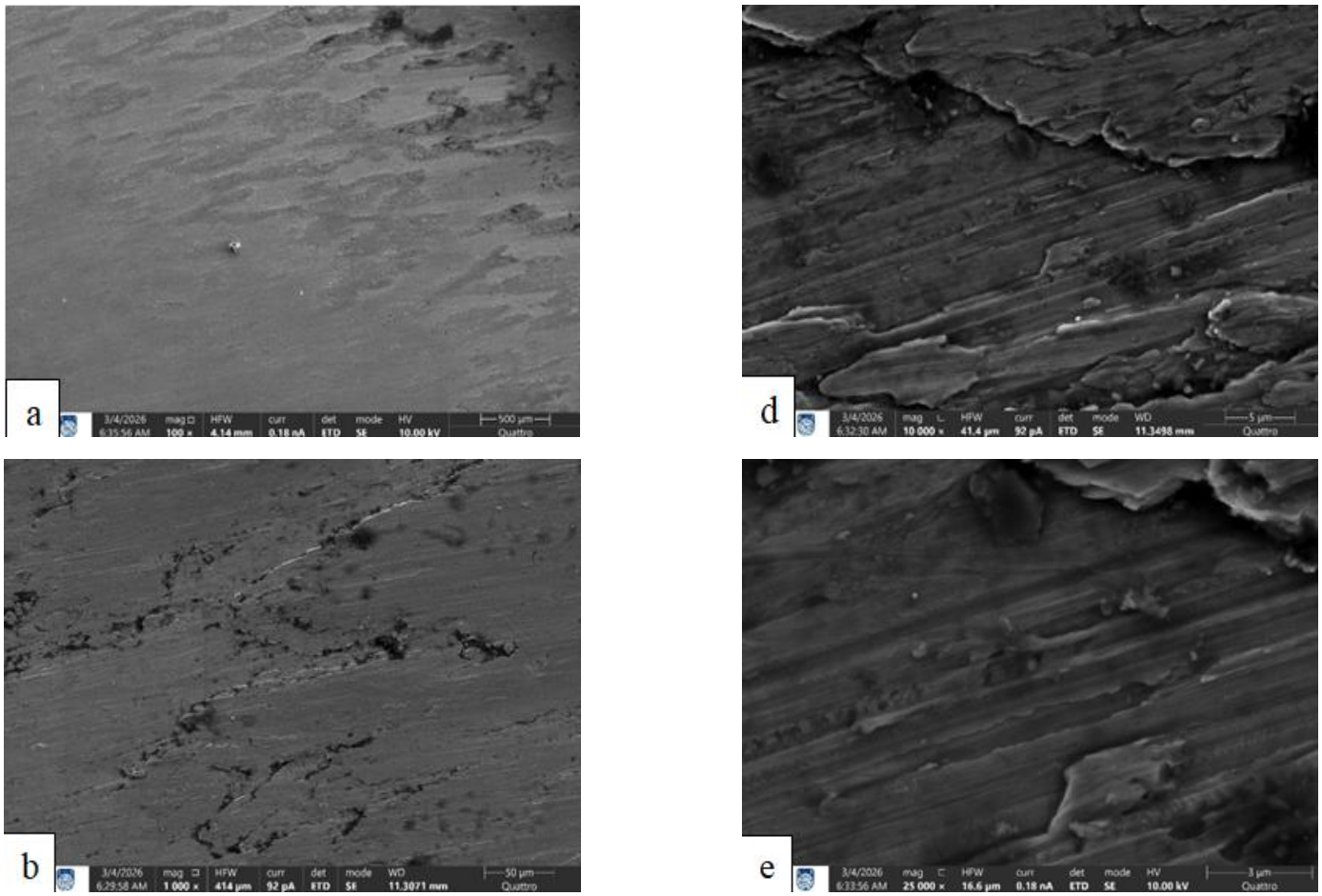

Fig. 2 Scanning electron microscope (SEM) images of the LPBF-fabricated sample before electron irradiation at different magnification levels. (a) 500 μm, (b) 50 μm, (c) 10 μm, (d) 5 μm, (e) 3 μm.

The morphology of the sample before irradiation is shown in Figure 2a–e. These images reveal that the material has a heterogeneous and highly agglomerated structure, with agglomerate sizes in the range of ≈50–100 μm. At medium magnification, particle sizes are in the range of 1–20 μm, while at high magnification, pore sizes are ≈0.2–1.0 μm, and the sizes of nanostructured features are in the range of ≈50–200 nm.

Figure 2a shows large irregular agglomerates distributed over the surface, indicating a heterogeneous microstructure formed during rapid solidification in the LPBF process. Figure 2b reveals numerous interparticle voids and insufficiently bonded regions, which are characteristic of lack-of-fusion defects. In Figure 2c, the rough particle morphology reflects the nonequilibrium crystallization conditions associated with high cooling rates. Figures 2d and 2e clearly demonstrate the presence of micropores and nanoscale structural features, which may act as stress concentration sites and negatively affect the mechanical performance of the alloy.

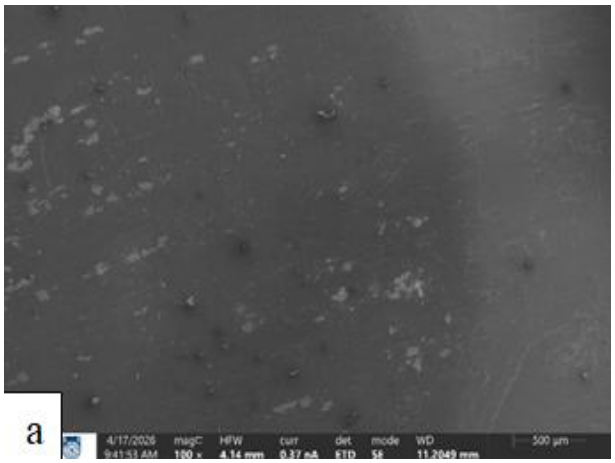

Fig. 3 Scanning electron microscope (SEM) images of the sample after electron irradiation at different magnification levels: (a) 500 μm, (b) 50 μm, (c) 20 μm, (d) 10 μm, (e) 5 μm.

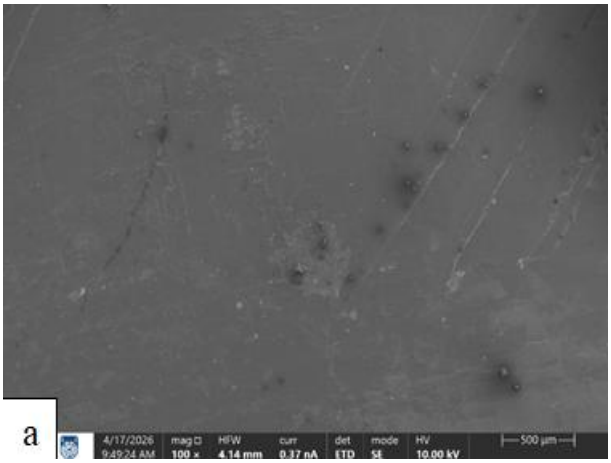

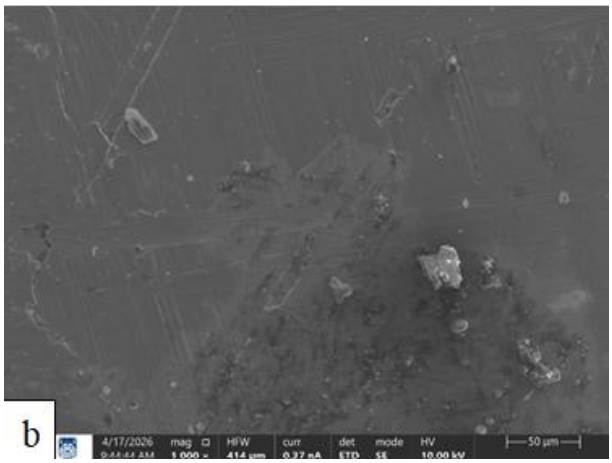

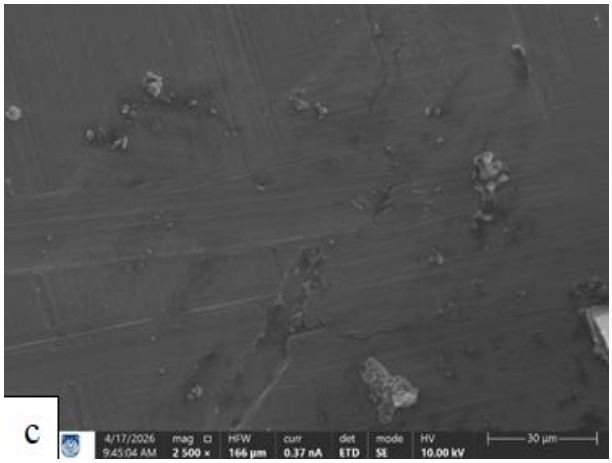

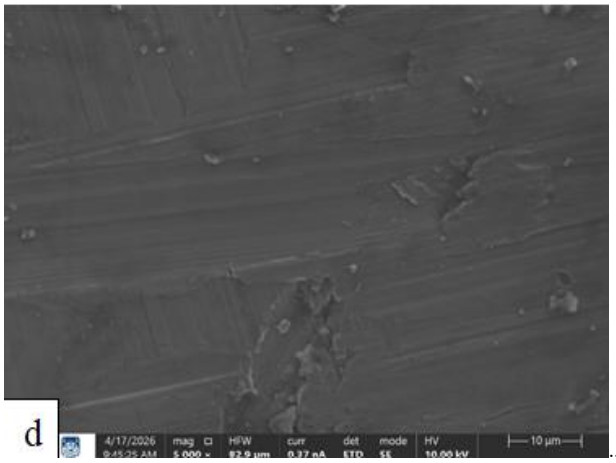

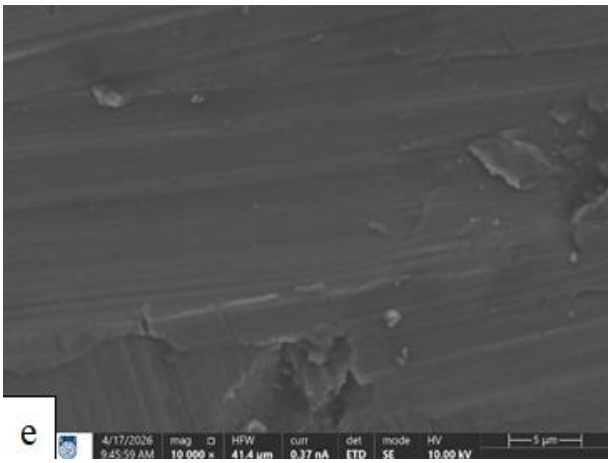

Fig. 4 Scanning electron microscope (SEM) images of the sample after electron irradiation at different magnification levels: (a) 500 µm, (b) 50 µm, (c) 30 µm, (d) 10 µm, (e) 5 µm.

The morphology after electron irradiation is shown in Figures 3a–e and 4a–e. In this case, the agglomerate size increases to ≈60–130 µm, which is an increase of ≈20–30%. At the same time, the proportion of contact zones between particles increases, indicating a densification of the structure. The pore sizes decrease to the range of ≈0.1–0.8 µm in Figures 3d–e and to ≈0.08–0.6 µm in Figures 4d–e. The observed increase in agglomerate size can be attributed to irradiation-induced diffusion processes and local thermal effects generated by the electron beam. The energy transferred by accelerated electrons increases atomic mobility in the near-surface region, promoting particle coalescence and the formation of larger agglomerates. Simultaneously, the enhanced diffusion flux facilitates material transport toward pore surfaces, leading to gradual pore shrinkage and densification of the structure. Such behavior is characteristic of thermally activated sintering processes occurring under nonequilibrium conditions.

In high-magnification images (Figure 3e and Figure 4e), a reorganization of nanostructured elements is observed; their sizes are in the range of ≈40–120 nm, and the degree of integration is ≈40–60%. The refinement and integration of nanoscale structural features indicate the occurrence of recovery and structural relaxation processes. Electron irradiation promotes the redistribution of crystal defects, including vacancies and dislocations, thereby reducing the overall defect density and surface energy. As a result, the system tends toward a more thermodynamically stable configuration characterized by improved structural compactness and stronger interparticle bonding. A detailed analysis of Figures 3a–e and 4a–e indicates that electron irradiation promotes progressive particle coalescence and defect healing. In Figures 3a and 3b, the reduction of open gaps between neighboring particles is observed, while Figures 3c and 4c show the formation of larger compact regions due to enhanced diffusion processes. At higher magnifications (Figures 3d–e and 4d–e), pore shrinkage and surface smoothing become evident, confirming the occurrence of irradiation-induced densification. These results prove that the processes of atomic diffusion and resintering occur intensively under the influence of electron irradiation.

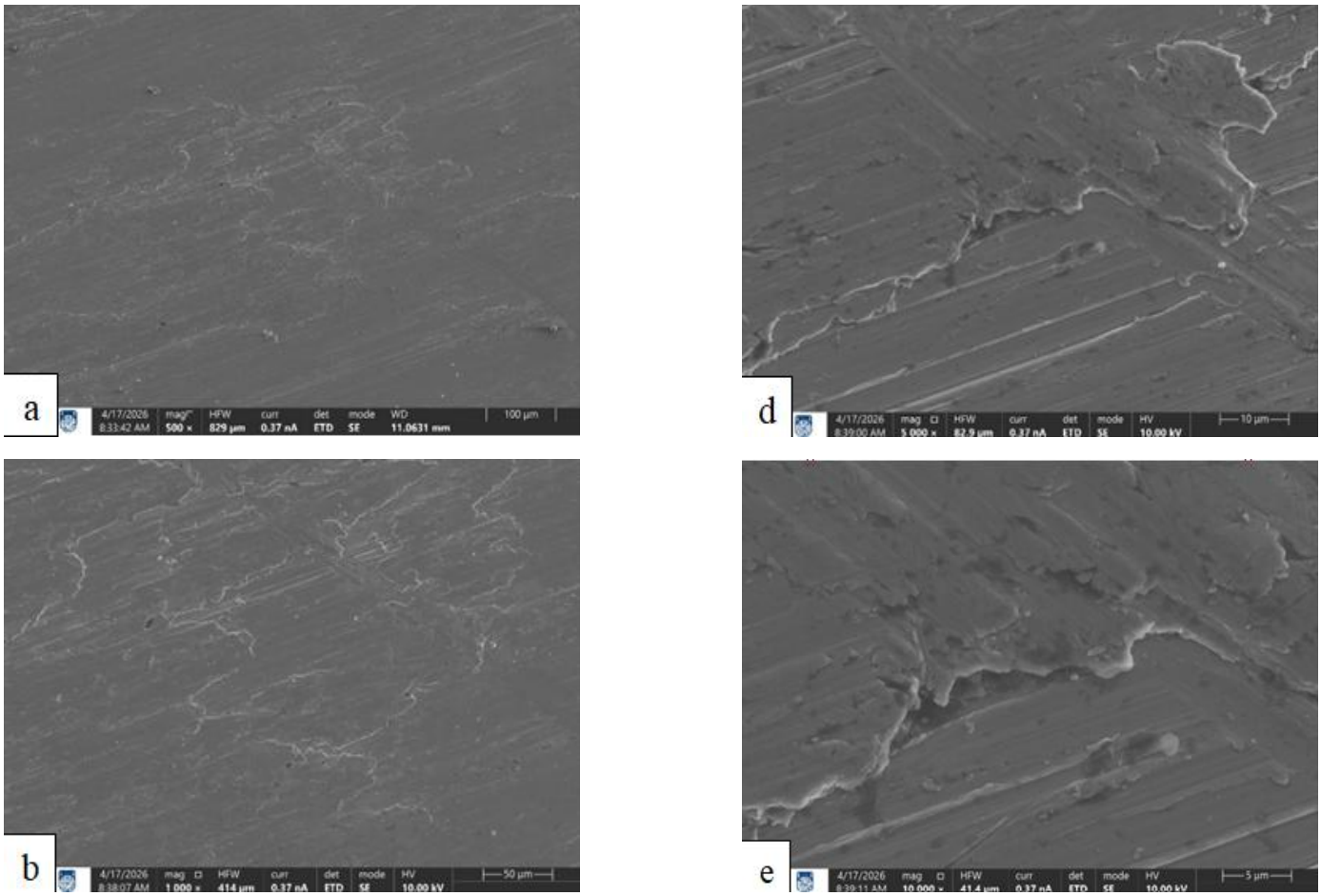

Fig. 5 Scanning electron microscope (SEM) images of the sample after electron irradiation at different magnification levels: (a) 100 μm, (b) 50 μm, (c) 30 μm, (d) 10 μm, (e) 5 μm.

The morphological features of the third region are shown in Figures 5a–5e. In this region, the agglomerate size increased to ≈80–150 μm, representing an increase of ≈30–50% compared to the initial state. At the same time, the porosity decreased from 0.2–1.0 μm to 0.05–0.5 μm, representing a decrease of ≈50–60%. Figure 5a demonstrates the formation of large compact agglomerates with a significantly reduced number of structural discontinuities. Figure 5b shows a lower density of visible pores compared to the initial state. In Figure 5c, particle boundaries become less distinct, indicating advanced coalescence processes. Figures 5d and 5e reveal a dense nanoscale morphology with minimal pore content, suggesting that prolonged electron irradiation promotes structural consolidation and defect elimination in the surface layer of the alloy. No evidence of irradiation-induced macrocracks, delamination, or severe surface degradation was observed in the SEM micrographs after electron irradiation. On the contrary, the reduction in pore size and the increased degree of particle coalescence indicate that the applied irradiation conditions promoted structural densification rather than defect formation. Nevertheless, the presence of nanoscale defects and residual stresses cannot be completely excluded and requires further investigation using high-resolution characterization techniques such as TEM and EBSD. In addition to the overall reduction in porosity, the pore-size distribution became noticeably narrower after irradiation. While the as-fabricated sample exhibited a broad distribution of pores ranging from approximately 0.2 to 1.0 μm, the irradiated material was characterized by a predominance of smaller pores within the range of 0.05–0.5 μm. This behavior suggests a more homogeneous microstructure and confirms the occurrence of diffusion-assisted pore closure and defect-healing processes during electron irradiation. The results of the elemental composition analysis are shown in the spectra in Figures 6 and 7. In the sample before irradiation (Figure 7), the Ti content was ≈83.9 at.%, whereas after irradiation (Figure 5), it decreased to ≈49.2 at.%. In addition, an increase in the carbon (≈22.8 at.%) and

oxygen (≈18.9 at.%) content was recorded, indicating oxidation and chemical modification processes on the surface of the material.

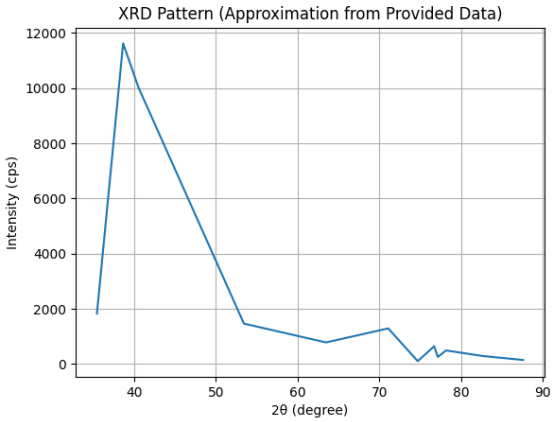

Fig. 6 X-ray diffraction (XRD) spectrum of the LPBF-fabricated sample before electron irradiation.

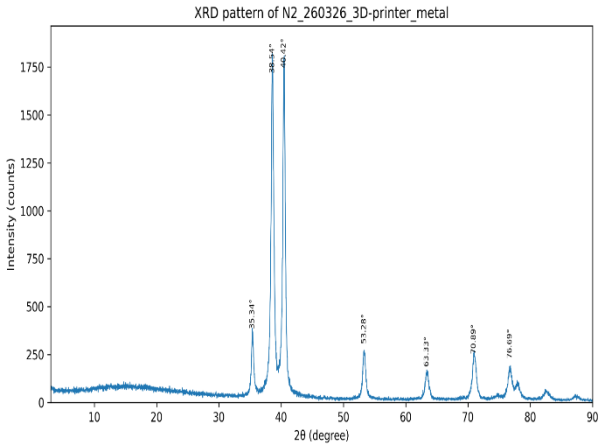

Fig. 7 X-ray diffraction pattern of the sample after irradiation (predominance of the Ti phase).

The results of the phase composition analysis are shown in the diffraction patterns in Figures 6 and 7. In the sample before irradiation (Figure 6), the main phase was determined to be the intermetallic compound Al_3Ti_{17}, whereas after irradiation (Figure 7), the Ti phase was predominant. The diffraction maxima are located in the range of 2θ ≈35–40°, which corresponds to the hexagonal structure of Ti. In addition, after irradiation, the lattice parameters changed: a = 2.927 Å increased from 2.936 Å, and c = 4.663 Å increased from 4.676 Å, which indicates the expansion of the crystal lattice and the redistribution of internal stresses (Figure 7). The observed phase evolution after electron irradiation can be explained by the relaxation of metastable structural states formed during the LPBF process. Due to the extremely high cooling rates associated with additive manufacturing, the Ti-6Al-4V alloy initially contains nonequilibrium phases and significant residual stresses. Electron irradiation supplies additional energy to the crystal lattice, promoting atomic diffusion and structural rearrangement. As a result, the phase composition tends toward a more thermodynamically stable state, which is reflected by the predominance of the Ti phase after irradiation. The changes in lattice parameters further support this interpretation. The slight variation of the a and c parameters indicates a redistribution of alloying elements and a partial relaxation of internal stresses generated during rapid solidification. Such behavior is typical for titanium alloys subjected to thermal or radiation-induced recovery processes, where defect density decreases and the crystal structure becomes more ordered.

The obtained results are consistent with previously reported studies on additively manufactured Ti-6Al-4V alloys and radiation-assisted structural modification. Similar heterogeneous microstructures containing agglomerates, micropores, and nonequilibrium structural features have been reported for LPBF-produced Ti-6Al-4V alloys by Laskowska et al. [5], Tang et al. [17], and Wang et al. [18]. According to these authors, the rapid solidification conditions associated with additive manufacturing lead to the formation of residual stresses, metastable phases, and structural defects, which is in agreement with the morphology observed in Figure 2. The reduction in porosity and the increase in agglomerate size observed after electron irradiation are consistent with the densification mechanisms reported by Wang et al. [34] and Zhang et al. [32]. These studies demonstrated that irradiation-induced diffusion and local thermal effects accelerate mass transport processes, resulting in pore shrinkage, particle coalescence, and structural consolidation. Similar behavior was observed in the present study, where pore sizes decreased from approximately 0.2–1.0 μm to 0.05–0.5 μm, while the agglomerate size increased by approximately 30–50%. The phase evolution detected by XRD is also consistent with previous investigations of titanium alloys subjected to thermal and irradiation treatments. Xu et al. [25], Zhou et al. [27], and Perevalova et al. [15] reported that additional energy input promotes structural relaxation, phase stabilization, and redistribution of alloying elements. The predominance of the Ti phase after irradiation and the observed changes in lattice parameters indicate a transition toward a more thermodynamically stable state, which agrees with the recovery mechanisms described in the literature.

Overall, a comparative analysis of the SEM (Figures 2, 3, 4, 5) and X-ray diffraction (Figures 6–7) results showed that electron irradiation has a multi-level effect on the structure of the Ti-6Al-4V alloy. The observed structural evolution can be explained by the combined thermal and radiation effects of the electron beam. Electron irradiation increases atomic mobility, accelerates diffusion-controlled mass transport, and promotes defect annihilation. As a result, particle coalescence, pore closure, and structural relaxation occur simultaneously, leading to a denser and more homogeneous microstructure. At the microscale, agglomerate coarsening and porosity reduction are observed, while at the nanoscale, particle coalescence and structural compaction occur.

Future research will focus on establishing quantitative relationships between electron irradiation parameters and the resulting structural evolution of Ti-6Al-4V alloys produced by LPBF. Particular attention will be devoted to the influence of irradiation on mechanical performance, including hardness, wear resistance, tensile properties, and fatigue behavior. In addition, advanced characterization techniques such as EBSD and TEM will be employed to investigate grain evolution, phase transformations, and irradiation-induced defect redistribution at the micro- and nanoscale levels.

It should be noted that the present study was primarily focused on the microstructural, chemical, and phase evolution of the Ti-6Al-4V alloy subjected to electron irradiation. Mechanical properties such as microhardness, tensile strength, fracture toughness, and fatigue resistance were not directly evaluated within the scope of this work. Therefore, although the observed reduction in porosity and structural densification suggest a potential improvement in mechanical performance, additional experimental studies are required to establish quantitative structure–property relationships.

Conclusions

In this paper, we comprehensively studied the structural and phase evolution of Ti-6Al-4V alloy fabricated by Laser Powder Bed Fusion (LPBF) under electron irradiation. The results of SEM, EDS, and XRD methods showed that significant changes in the morphology, chemical composition, and phase state of the material occur at the micro- and nanoscale. SEM analysis showed that after electron irradiation, the agglomerate size increased from ≈50–100 μm to 70–150 μm (≈20–40%), and the porosity decreased from ≈0.2–1.0 μm to 0.05–0.6 μm (≈40–60%). At the same time, the size of nanostructured elements changed from ≈50–200 nm to the range of 30–120 nm, and the degree of their integration reached ≈40–70%. These changes indicate structural densification associated with enhanced atomic diffusion and resintering processes.

Energy dispersive X-ray diffraction (EDS) analysis revealed a decrease in the Ti content from ≈83.9 at.% to ≈49.2 at.% after irradiation and an increase in the oxygen (≈18.9 at.%) and carbon (≈22.8 at.%) contents. This indicates active oxidation and adsorption processes on the material surface. X-ray diffraction (XRD) analysis clearly confirmed the phase changes: while intermetallic Al–Ti phases predominated in the initial state, the predominant formation of the hexagonal Ti phase was detected after irradiation. Furthermore, the change in lattice parameters (a: 2.927 → 2.936 Å, c: 4.663 → 4.676 Å) indicates lattice expansion and redistribution of internal stresses. The obtained results indicate that electron irradiation significantly affects the surface and near-surface structural state of the LPBF-produced Ti-6Al-4V alloy, leading to morphological densification and changes in phase composition. However, the observed variations in elemental composition, particularly the increase in oxygen and

carbon content, are likely influenced by surface-sensitive measurement conditions and should be interpreted with caution.
Furthermore, the contribution of thermal effects during irradiation cannot be fully excluded and may play a role in the observed structural transformations. Therefore, the presented results should be considered as indicative of combined irradiation–thermal effects rather than purely radiation-induced phenomena.
The established microstructural modifications suggest a potential impact on material properties; however, further investigation is required to quantitatively assess the relationship between processing conditions, structure, and functional performance.

Acknowledgement: This research was funded by the Science Committee of the Ministry of Science and Higher Education of the Republic of Kazakhstan (grant No. AP26198529).

REFERENCES

1. T. DebRoy, et al.: Progress in Materials Science, 92, 2018, 112-224. https://doi.org/10.1016/j.pmatsci.2017.10.001.
2. D. Herzog, V. Seyda, E. Wycisk, C. Emmelmann: Acta Materialia, 117, 2016, 371-392, https://doi.org/10.1016/j.actamat.2016.07.019.
3. C. Ni, et al.: Recent advances in LPBF Ti-6Al-4V. Additive Manufacturing, 20(1), 2025, e2446952, https://doi.org/10.1080/17452759.2024.2446952.
4. C. García-Hernández, et al.: Scientific Reports, 15, 2025, 14087. https://doi.org/10.1038/s41598-025-98349-6
5. D. Laskowska et al.: Materials, 17, 2024, 4604. https://doi.org/10.3390/ma17184604
6. L. Wu et al.: Journal of Materials Research and Technology, 35, 2025, 176-184. https://doi.org/10.1016/j.jmrt.2025.01.012
7. A.K.S. Chauhan, et al.: Journal of Materials Engineering and Performance, 33, 2024, 12806-12818. https://doi.org/10.1007/s11665-024-09935-0
8. A.J. Sterling, et al.: Materials Science and Engineering: A, 655, 2016, 100-112. https://doi.org/10.1016/j.msea.2015.12.026
9. S.M. Kelly, S.L. Kampe: Metallurgical and Materials Transactions A, 35, 2004, 1861–1867. https://doi.org/10.1007/s11661-004-0094-8
10. B. Vrancken, et al.: Journal of Alloys and Compounds, 541, 2012, 177-185. https://doi.org/10.1016/j.actamat.2020.10.052
11. T. Ahmed, H.J. Rack: Materials Science and Engineering: A, 243, 1998, 206-211. https://doi.org/10.1016/S0921-5093(97)00802-2
12. S. Liu, Y.C. Shin: Materials & Design, 164, 2019, 107552. https://doi.org/10.1016/j.matdes.2018.107552
13. S.J. Zinkle, G.S. Was: Radiation Effects in Materials. In: *Comprehensive Nuclear Materials*. 2. ed. Oxford: Elsevier, 2022, p. 20–70. https://doi.org/10.1016/B978-0-12-803581-8.11624-9
14. G.S. Was: *Fundamentals of radiation materials science: Metals and Alloys*. 2. ed. New York: Springer. https://doi.org/10.1007/978-3-540-49472-0
15. O.B. Perevalova et al. Physics of Metals and Metallography, 125(7), 2024, 898-905. https://doi.org/10.31857/S0015323024070105
16. A.D. Boccardo et al. Applied Physics, 2024. https://doi.org/10.48550/arXiv.2404.09806
17. L. Wang et al. Materials & Design, 256, 2025, 114235. https://doi.org/10.1016/j.matdes.2025.114235
18. R. Xu et al.: Materials Today Communications, 35, 2023, 105571. https://doi.org/10.1016/j.mtcomm.2023.105571
19. X.F. Fu et al. Journal of Materials Research and Technology, 18, 2022, 1155-1165. https://doi.org/10.1016/j.jmrt.2022.03.021
20. J. Niu et al. Materials Science and Engineering: A, 922, 2025, 147611. https://doi.org/10.1016/j.msea.2024.147611
21. S. Su et al. Materials Science and Engineering: A, 874, 2023, 145085. https://doi.org/10.1016/j.msea.2023.145085
22. L. Jou et al. Journal of Alloys and Compounds, 1064, 2026, 188014. https://doi.org/10.1016/j.jallcom.2026.188014
23. J. Bidulská, R. Bidulský, M. Actis Grande, T. Kvačkaj: Materials, 12, 2019, 3724. https://doi.org/10.3390/ma12223724
24. R. Bidulsky, J. Bidulska, F.S. Gobber, T. Kvackaj, P. Petrousek, M. Actis-Grande, K.P. Weiss, D. Manfredi: Materials, 2020, 13, 3328. https://doi.org/10.3390/ma13153328
25. Ľ. Kaščák, J. Varga, J. Bidulská, R. Bidulský, M. A. Grande: Acta Metallurgica Slovaca, 29(2), 2023, 113-118. https://doi.org/10.36547/ams.29.2.1846
26. R. Bidulsky, F.S. Gobber, J. Bidulska, M. Ceroni, T. Kvackaj, M. A. Grande: Metals, 11(11), 2021, 1831. https://doi.org/10.3390/met11111831
27. Ch.Ch. Liu et al. Transactions of Nonferrous Metals Society of China, 34(10), 2024, 3093-3117. https://doi.org/10.1016/S1003-6326(24)66597-0
28. A. Di Schino, G. Stornelli: Acta Metallurgica Slovaca, 28(4), 2022, 208-211. https://doi.org/10.36547/ams.28.4.1648
29. H Yang, et al.: Journal of Nuclear Materials, 561, 2022, 153571. https://doi.org/10.1016/j.jnucmat.2022.153571
30. S.J. Zinkle, G.S. Was: Acta Materialia, 61(3), 2013, 735-758. https://doi.org/10.1016/j.actamat.2012.11.004
31. P. Hosemann, D. Frazer, M. Fratoni, A. Bolind, M.F. Ashby: Scripta Materialia, 143, 2018, 181-187. https://doi.org/10.1016/j.scriptamat.2017.04.027
32. Y. Zhang et al. Surface and Coatings Technology, 477, 2024, 130387. https://doi.org/10.1016/j.surfcoat.2024.130387
33. S. Zhang et al. Nuclear Instruments and Methods in Physics Research Section B: Beam Interactions with Materials and Atoms, 543, 2023, 165097. https://doi.org/10.1016/j.nimb.2023.165097
34. Y. Xia et al. Materials Science and Engineering: A, 559, 2013, 293-300. https://doi.org/10.1016/j.msea.2012.08.100
35. K. Gautier, et al. Computational Materials Science, 259, 2025, 114197. https://doi.org/10.1016/j.commatsci.2025.114197